Materials Today Chemistry 9 (2018) 17–27

Contents lists available at ScienceDirect

Materials Today Chemistry

journal homepage: www.journals.elsevier.com/materials-today-chemistry/

Atomic layer deposition of crystalline molybdenum oxide thin films and phase control by post-deposition annealing

Miika Mattinen [a, *], Peter J. King [a], Leonid Khriachtchev [a, 1], Mikko J. Heikkilä [a], Ben Fleming [b], Simon Rushworth [b], Kenichiro Mizohata [c], Kristoffer Meinander [c], Jyrki Räisänen [c], Mikko Ritala [a], Markku Leskelä [a]

[a] Department of Chemistry, University of Helsinki, P.O. Box 55, FI-00014, Finland
[b] EpiValence Ltd, The Wilton Centre, Redcar, Cleveland, TS10 4RF, UK
[c] Division of Materials Physics, Department of Physics, University of Helsinki, P.O. Box 43, FI-00014, Finland

ARTICLE INFO

Article history:
Received 9 March 2018
Received in revised form
11 April 2018
Accepted 30 April 2018
Available online 11 May 2018

Keywords:
Atomic layer deposition
Molybdenum oxide
MoO_3
MoO_2
Thin films

ABSTRACT

Molybdenum forms a range of oxides with different stoichiometries and crystal structures, which lead to different properties and performance in diverse applications. Herein, crystalline molybdenum oxide thin films with controlled phase composition are deposited by atomic layer deposition. The $MoO_2(thd)_2$ and O_3 as precursors enable well-controlled growth of uniform and conformal films at 200–275 °C. The as-deposited films are rough and, in most cases, consist of a mixture of α- and β-MoO_3 as well as an unidentified suboxide MoO_x ($2.75 \leq x \leq 2.89$) phase. The phase composition can be tuned by changing deposition conditions. The film stoichiometry is close to MoO_3 and the films are relatively pure, the main impurity being hydrogen (2–7 at-%), with ≤1 at-% of carbon and nitrogen. Post-deposition annealing is studied *in situ* by high-temperature X-ray diffraction in air, O_2, N_2, and forming gas (10% H_2/90% N_2) atmospheres. Phase-pure films of MoO_2 and α-MoO_3 are obtained by annealing at 450 °C in forming gas and O_2, respectively. The ability to tailor the phase composition of MoO_x films deposited by scalable atomic layer deposition method represents an important step towards various applications of molybdenum oxides.

1. Introduction

Molybdenum oxides (MoO_x) form a versatile group of materials as their properties vary widely as a function of the molybdenum oxidation state [1]. The most common molybdenum oxides are the monoclinic dioxide (MoO_2) and the trioxide (MoO_3), the latter of which exists in stable orthorhombic α and metastable monoclinic β phases. In addition, many crystalline mixed-valence suboxides with compositions between $MoO_{2.75}$ and MoO_3 are known, including the γ and η phases of Mo_4O_{11} ($x = 2.75$), $Mo_{17}O_{47}$ ($x \approx 2.76$), Mo_5O_{14} ($x = 2.80$), and Mo_8O_{23} ($x \approx 2.88$) as well as Mo_9O_{26} ($x \approx 2.89$) in the monoclinic and triclinic ("$Mo_{18}O_{52}$") phases [2–4]. The versatility of molybdenum oxides is reflected in, for example, the electrical properties at room temperature: α and β-MoO_3 are relatively insulating with band gaps of approximately 3 eV [5] (resistivity usually $>10^9$ Ωcm) [5–7], Mo_9O_{26} is a semiconductor ($\rho \approx 100$ Ωcm) [2,8], whereas γ-Mo_4O_{11} ($\rho \approx 10^{-4}$ Ωcm) [8,9] and the well-known MoO_2 ($\rho \approx 10^{-4}$ Ωcm) [10] are highly conducting. Additionally, oxygen vacancies or reactions with hydrogen occur easily for MoO_3, leading to oxygen deficient, n-type semiconductor MoO_{3-y} or hydrogen bronzes H_zMoO_3. Partial reduction of molybdenum is accompanied by an increase in electrical conductivity [4,11–14]. Amorphous MoO_x is also common with varying stoichiometries and, consequently, with different properties [15–17].

Due to the possible changes in the structure and oxidation state of molybdenum, molybdenum oxides show changes in optical properties upon excitation by light, heat, or applied voltage, i.e., photochromism [13,15,16,18], thermochromism [18,19], and electrochromism [15], respectively. The most widely studied applications of the chromatic phenomena lie in smart windows and other optical coatings [20], but chromatic metal oxides may also be useful for displays and optical memories, for example [21,22]. Other applications for MoO_3 and MoO_{3-y} include catalysis [23,24], gas sensors [25], resistive switching memories [26], and lithium ion

* Corresponding author.
E-mail address: miika.mattinen@helsinki.fi (M. Mattinen).
[1] Dedicated in memory of Dr. Leonid Khriachtchev.

https://doi.org/10.1016/j.mtchem.2018.04.005

batteries [27]. Notably, α-MoO_3 has a two-dimensional crystal structure and a larger band gap than the most known 2D materials, such as transition metal dichalcogenides akin to MoS_2. The 2D α-MoO_3 has shown promise as a channel [11], contact [28], and electron acceptor [29] material in field-effect transistors. In gas sensors the 2D α-MoO_3 has shown enhanced performance over its bulk counterpart [30]. Many of the applications of MoO_2 are similar to those of MoO_3 and MoO_{3-y}, including catalysis [31] or lithium ion batteries [32]. Reported applications of the crystalline suboxides with $2.75 \leq x \leq 2.89$ are quite sparse, but some investigations have been made regarding lithium ion batteries [33–35] and catalysis [36,37].

Different MoO_x phases show varying performance in different applications. For example, the layered structure of α-MoO_3 allows it to outperform β-MoO_3 in gasochromic applications [38], whereas β-MoO_3 has been suggested to be more active for catalytic oxidation of methanol [39]. Oxygen-deficient MoO_{3-y} has also been proposed to exhibit higher activity than MoO_3 in some photo- and electrocatalytic applications [1,40]. It has also been suggested that the crystalline suboxides may, at least in some cases, be the actual active species in catalysts considered to be MoO_3 [36]. In addition to the phase, film morphology is often crucial; in particular, high roughness or porosity of MoO_x has been found beneficial for electrocatalysis, gas sensors, and lithium ion batteries, among other applications [40–43].

For many of the abovementioned applications, either uniform thin films or nanoparticles with controlled sizes and morphologies are required. Atomic layer deposition (ALD) is an advanced gas phase thin film deposition method, which relies on alternating self-limiting surface reactions. Therefore, ALD is able to coat large areas as well as substrates with complex shapes with a thickness uniformity unmatched by any other method. ALD also typically deposits high-quality films at relatively low deposition temperatures. In addition, due to the cyclic nature of ALD, film thickness and doping can be controlled accurately [44–46].

Reports on ALD of metal oxides have been very common since the 1990s, but the first report on the ALD of molybdenum oxide was published as late as in 2011 by Diskus et al. [47], who used $Mo(CO)_6$ with "wet ozone", i.e. simultaneous exposure to O_3 and H_2O, as the reactant. Since 2014, a range of new MoO_x processes have been published, including $Mo(CO)_6$ with O_2 plasma [48], $Mo(N^tBu)_2(NMe_2)_2$ with either O_3 [49] or O_2 plasma [50,51], $MoO_2(^tBuAMD)_2$ with O_3 [52], $MoO_2(^iPrAMD)_2$ with O_3 [53], $Mo(CpSiMe_3)(CO)_2$(2-methylallyl) with O_3 [54] as well as the only H_2O-based process, Mo(ethylbenzene)$_2$ with H_2O [55]. The composition of the deposited films, if reported, has usually been close to MoO_3 [47,49–51,53,54,56], except for the Mo(VI)oxynitride films deposited from $MoO_2(^tBuAMD)_2$ and O_3 [52].

Deposition of crystalline (α-MoO_3) films by ALD has only been reported from $Mo(N^tBu)_2(NMe_2)_2$ and O_2 plasma at 250 °C and above [51]. Diskus et al. [56] managed to crystallize the initially amorphous MoO_x films deposited from $Mo(CO)_6$ and wet O_3 to either α-MoO_3 or a mixture of α- and β-MoO_3 depending on the annealing temperature. Nevertheless, the aforementioned approaches to produce crystalline films rely on either the use of plasma, which is problematic regarding conformality as well as batch processing, or post-deposition annealing, which is not suitable for temperature-sensitive substrates. Furthermore, to the best of our knowledge, neither MoO_2 nor any of the crystalline suboxide phases ($2.75 \leq x \leq 2.89$) have been achieved by ALD, with or without post-deposition annealing. More generally, reports on thin films of the suboxides are also scarce, which hinders their application.

We report the first ALD process capable of depositing crystalline molybdenum oxide films without the use of plasma, using a new ALD precursor $MoO_2(thd)_2$ with O_3 as the reactant. The growth characteristics were studied, followed by detailed film characterization. Post-deposition annealing experiments were performed using *in situ* high-temperature X-ray diffraction in both reducing and oxidizing atmospheres. Annealing was then optimized to produce phase-pure films of α-MoO_3 and MoO_2.

2. Experimental

2.1. Film deposition

Molybdenum oxide thin films were deposited using a commercial, hot wall flow-type F120 ALD reactor [57]. Nitrogen (N_2, AGA, 99.999%) was used as both carrier and purge gas at a flow rate of 400 sccm. The reactor pressure was on the order of 5 mbar. The deposition temperature varied by no more than ±2 °C during each deposition, mostly towards higher temperatures due to overshoot during heating of the reactor. The films were deposited on 5×5 cm^2 silicon (100) and soda lime glass substrates. The glass substrates were cleaned in an ultrasonic bath using successive baths of an alkaline ultrasonic cleaning solution, ethanol, and deionized water. The silicon wafers were used as-received.

Dioxobis(2,2,6,6-tetramethylheptane-3,5-dionato)molybdenum(VI) ($MoO_2(thd)_2$, 99.5%, EpiValence) was evaporated from an open glass boat heated to 135 °C inside the ALD reactor, slightly above the melting point of the precursor, which was about 130 °C under the ALD reactor conditions. A Mettler Toledo STARe system equipped with a TGA850 thermobalance was used for simultaneous thermogravimetric analysis (TGA) and differential thermal analysis (DTA) of the precursor. The TGA/DTA measurement was performed at atmospheric pressure of flowing N_2 using a heating rate of 10 °C/min and a sample size of approximately 10 mg.

Ozone (O_3) was produced from oxygen (O_2, AGA, 99.999%) using an ozone generator (Wedeco Ozomatic Modular 4 HC). The nominal O_3 concentration was 100 g/Nm^3 and the flow rate of the O_3–O_2 mixture was typically set to approximately 200 sccm using a needle valve. Unless otherwise noted, films were deposited at 250 °C using 1 s $MoO_2(thd)_2$ and 3 s O_3 pulses separated by 1 s N_2 purges.

2.2. Thickness measurements

Film thicknesses were measured by ellipsometry using a Film Sense FS-1 Multi-Wavelength instrument. The model used to fit the data consisted of four layers (silicon, native silicon oxide, dense MoO_x bottom layer, and rough MoO_x top layer). The rough top layer was necessary to obtain good agreement between the data and the model and it was implemented using an effective medium approximation with 50% of the layer being void and the other 50% having properties of the dense MoO_x layer underneath. Cauchy model was used for layers other than the silicon substrate. For comparison, UV–VIS spectroscopy (Hitachi U2000) and energy-dispersive X-ray spectrometry (EDS, Oxford INCA 350 connected to Hitachi S-4800) were also used for some samples to confirm the thicknesses measured by ellipsometry. The high roughness of most films prevented the use of X-ray reflectivity (XRR).

2.3. Film characterization

Film morphology was studied by scanning electron microscopy (SEM, Hitachi S-4800) and atomic force microscopy (AFM, Veeco Multimode V). AFM imaging was done in the tapping mode in air using silicon probes (Bruker) with a nominal tip radius of less than 10 nm. The images were flattened to remove artefacts caused by sample tilt and scanner nonlinearity. Film roughness was calculated as a root mean square value (R_q) from 2×2 μm^2 images.

Film crystallinity was examined by X-ray diffraction (XRD) using a PANalytical X'Pert Pro MPD instrument in grazing incidence (incident angle of 1°) geometry and a Cu Kα (λ = 1.54 Å) X-ray beam. Composition of the surface layers was analyzed by X-ray photoelectron spectroscopy (XPS) using an Argus spectrometer (Omicron NanoTechnology GmbH). The samples were illuminated with X-rays emitted from a standard Mg source (Kα line) at a photon energy of 1253.6 eV. Binding energies were calibrated using the C 1s peak (284.8 eV) of ambient hydrocarbons, and peak fitting was done using the CasaXPS software. Film composition was analyzed by time-of-flight elastic recoil detection analysis (ToF-ERDA) using a 40 MeV $^{127}I^{7+}$ ion beam [58].

Micro-Raman spectra were measured in backscattering geometry using confocal Raman microscopes with 100× objectives. Measurements with a 325 nm laser were performed with a Horiba Jobin Yvon LabRam HR 800 instrument, whereas an NT-MDT Ntegra instrument was used with 532 nm and 633 nm lasers. Laser power was adjusted to a level where no deterioration of the sample occurred.

Optical transmission measurements of the films deposited on soda lime glass substrates were conducted using a Hitachi U-2000 UV–Vis spectrophotometer.

2.4. High-temperature X-ray diffraction

In situ high-temperature XRD (HTXRD) measurements were performed using an Anton-Paar HTK1200N oven connected to a PANalytical X'Pert Pro MPD diffractometer with a Cu Kα (λ = 1.54 Å) X-ray source. The measurements were done under atmospheric pressure of air, O_2 (AGA, 99.9999%), N_2 (AGA, 99.999%, further purified with an Entegris Gatekeeper purifier), or forming gas (10% H_2 in N_2, AGA). During the experiments, the temperature was increased from 26 up to 666 °C with the temperature stabilized every 40 °C for recording of a grazing incidence diffractogram (incident angle of 1°). Recording each diffractogram took approximately 35 min, and the heating between the measurements was done with a rate of 10 °C/min followed by a two minute stabilization period, which resulted in a total duration of approximately 11 h for each HTXRD experiment.

The Anton-Paar oven was also used to produce annealed films for further analysis. Based on the HTXRD measurements, a temperature of 450 °C and an annealing time of 1 h (O_2) or 3 h (forming gas) were selected. The heating rate was 10 °C/min, whereas cooling to room temperature took approximately 30 min. Isothermal measurements with consecutively measured grazing incidence diffractograms were also done under similar conditions to follow the transformation processes in more detail.

3. Results and discussion

3.1. Film growth

Molybdenum oxide thin films were deposited by atomic layer deposition (ALD) using dioxobis(2,2,6,6-tetramethylheptane-3,5-dionato)molybdenum(VI) [$MoO_2(thd)_2$] and O_3 as precursors. No appreciable film growth occurred using H_2O or H_2S as the reactant. The lack of reactivity with water is common for precursors containing β-diketonate ligands. In contrast, some of them, including $Mo(thd)_3$ [59], have been found to react with H_2S. To the best of our knowledge, $MoO_2(thd)_2$ is a new ALD precursor, whereas it has been used for CVD of MoO_x with O_2 as a reactant at relatively high temperatures (350–430 °C) [60].

Thermogravimetric analysis (TGA) showed that $MoO_2(thd)_2$ volatilized cleanly leaving a residue of less than 2% (Fig. 1). While a solid at room temperature, $MoO_2(thd)_2$ melted at approximately

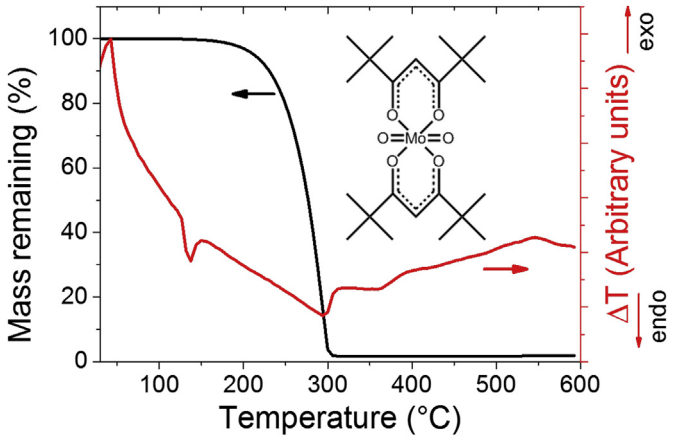

Fig. 1. Thermogravimetric analysis (TGA, black) and differential thermal analysis (DTA, red) data for $MoO_2(thd)_2$ (structure shown as inset) heated under atmospheric pressure of N_2.

130 °C, which is just below the source temperature used in this work and in agreement with literature values of 129–135 °C [61,62], as indicated by DTA (Fig. 1) and visual observations during heating of the ALD reactor. The favorable thermal properties together with the commercial availability and reactivity with O_3 make $MoO_2(thd)_2$ an attractive ALD precursor.

Most film growth experiments were done at 250 °C, the temperature which yielded the most uniform films and the highest growth rates close to 1 Å/cycle. Due to the roughness of the films, measuring film thicknesses turned out to be rather challenging by ellipsometry and UV–VIS spectrometry, and impossible by XRR. However, a good fit of the ellipsometry data was obtained by using a four-layer model consisting of a Si substrate, a native SiO_x layer, a dense MoO_x layer, and a rough MoO_x surface layer (Fig. 2a). Similar thickness values were also measured by UV–VIS spectrometry and EDS (Fig. S1, Supplementary data). The similar trends of the optical thicknesses (ellipsometry, UV–VIS) and the mass thicknesses (EDS) support the use of the ellipsometry-derived total film thicknesses, including both the dense bottom layer and the rough top layer, in the following discussion.

A rather high growth rate of approximately 1.0 Å/cycle was reached with a $MoO_2(thd)_2$ pulse of only 0.2 s (Fig. 2b). However, increasing the pulse length above 1.0 s led to a slight increase in the growth rate, which is likely due to precursor decomposition. Nevertheless, pulsing $MoO_2(thd)_2$ alone for 1000 pulses of 1 s each resulted in no film growth to the accuracy of the thickness measurements. Thus, the precursor decomposition seems to occur mostly on the surface of the growing MoO_x film as opposed to decomposition in the gas phase. From the average slope of the growth rate versus $MoO_2(thd)_2$ pulse length from 0.2 to 3.0 s the decomposition was estimated to increase the growth rate by approximately 0.1 Å/cycle per second of $MoO_2(thd)_2$ pulsing. Therefore, the decomposition contributed only 2% of the growth rate when using 0.2 s pulses, which already appeared to be long enough to saturate the ALD-like surface reactions. Furthermore, the deposited films were uniform over the 5 × 5 cm^2 substrates with non-uniformities below 5%. With ozone, a 2 s pulse was needed to reached saturated growth rate (Fig. 2c).

Interesting effects were observed when the film thickness was varied: during the first 100 cycles the film growth was linear but slow with a growth rate of 0.35 Å/cycle and no apparent nucleation delay (Fig. 2d). The growth was also linear between 250 and 1000 cycles, but with a much higher growth rate of 1.25 Å/cycle. Furthermore, the thinnest films could be modeled as a single, dense

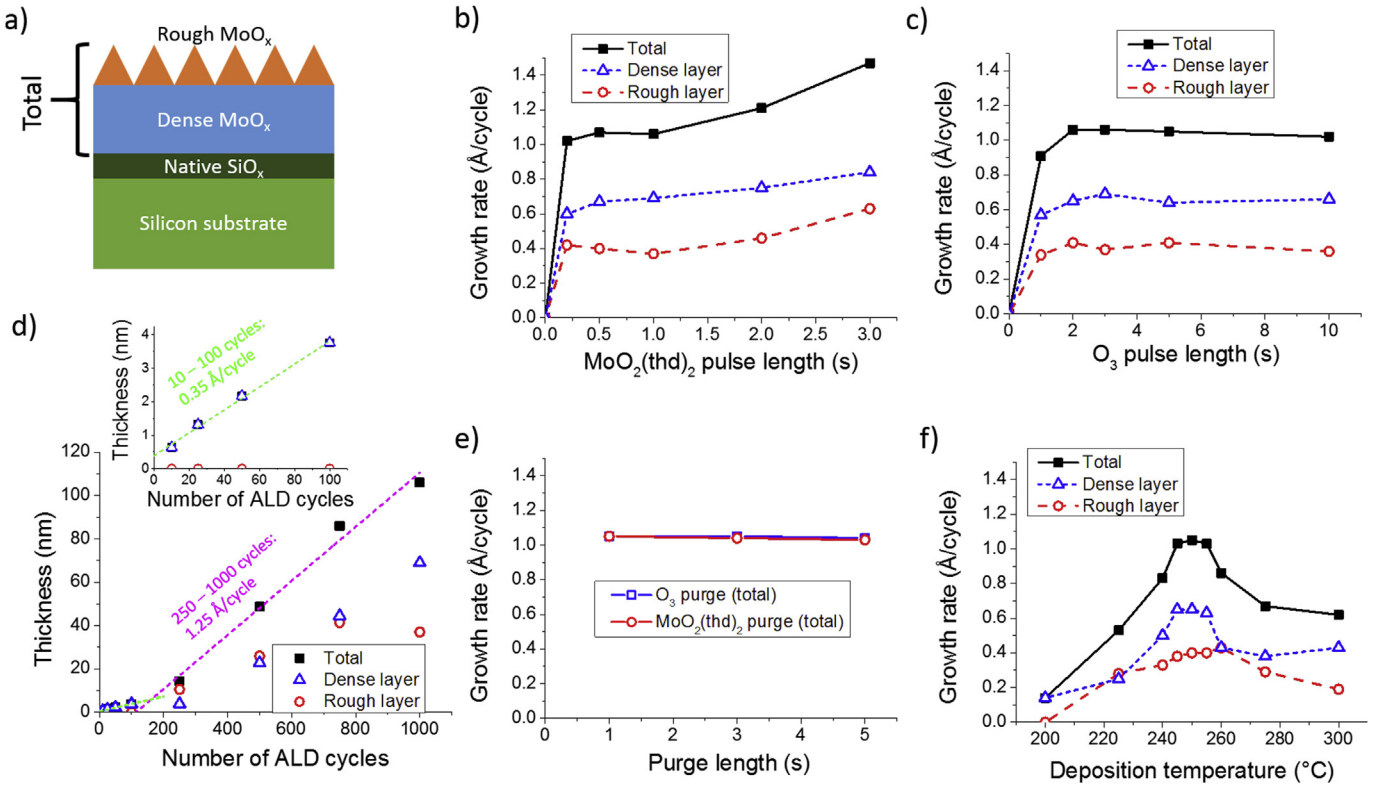

Fig. 2. (a) Illustration of the ellipsometry model used in this work. Growth rates versus (b) $MoO_2(thd)_2$ and (c) O_3 pulse lengths. (d) Film thickness versus the number of ALD cycles (inset shows 0–100 cycles). Growth rates extracted from linear fits to the data are indicated. Growth rates versus (e) purge lengths (only total thickness is shown for clarity) and (f) deposition temperature. Unless otherwise noted, 1000 cycles with 1 s $MoO_2(thd)_2$ and 3 s O_3 pulses and 1 s purges were applied at 250 °C.

layer, whereas the thicker films required a rough surface layer in the model. The dramatic increase in roughness and growth rate between 100 and 250 cycles is linked to crystallization of the films, as will be discussed in Section 3.2. Indeed, Vos et al. [51] noted a similar effect with their ALD MoO_x films grown from Mo(N-^{t}Bu)$_2$(NMe$_2$)$_2$ and O_2 plasma at 300 °C, although they measured a growth rate increase of only 25% upon crystallization compared to the 250% increase measured here. The difference may at least partly be explained by the high roughness of our films as well as the different chemical reactions in thermal versus plasma-enhanced ALD. Large, 1.4–4-fold increases in growth rates upon crystallization have also been observed with ALD TiO_2 films, which has been suggested to be due to both increased roughness and differences in surface chemistry, such as hydroxyl group coverage [63–65].

Varying the purge times from 1 to 5 s after each precursor pulse had no effect on the growth rate (Fig. 2e), as is expected for ALD. Pulse times of 1 s for $MoO_2(thd)_2$, 3 s for O_3, and purges of 1 s were selected for further experiments.

The film growth was rather sensitive to the deposition temperature, with the highest growth rates of approximately 1.0–1.1 Å/cycle observed between 245 and 255 °C (Fig. 2f). The growth rate decreased strongly on both sides of this temperature range, which is attributed to slower crystallization at temperatures below 245 °C and, possibly, changes in the crystalline phase composition for films deposited at temperatures above 255 °C. The latter would require different phases to have different growth rates, perhaps due to differing catalytic activity or hydroxyl group coverage. Additionally, the surface area of the films may change with deposition temperature, which would affect the growth rate. The films deposited at 300 °C showed increased non-uniformity, whereas films deposited at other temperatures were visibly uniform over the 5 × 5 cm^2 substrates used in this work. Furthermore, despite the slight precursor decomposition at 250 °C, highly conformal films were deposited on trenches with a high aspect ratio of 30:1 within the uncertainty of the thickness measurements of approximately ±5 nm (Fig. 3).

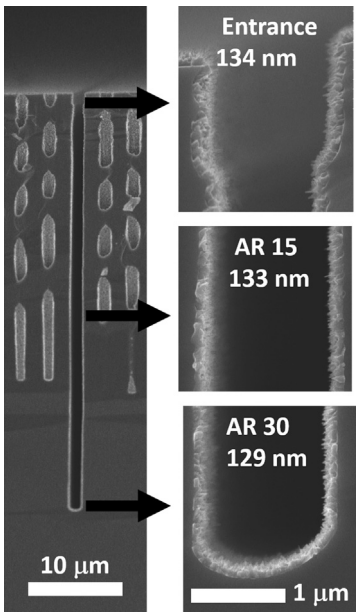

Fig. 3. Cross-sectional SEM images of a trench structure (aspect ratio 30:1) conformally coated with a MoO_x film. The film was deposited at 250 °C using 1 s $MoO_2(thd)_2$ and 5 s O_3 pulses and 5 s purges to ensure completion of surface reactions and purges in the deep structures.

3.2. Characterization

The film crystallinity was first examined by XRD. For an approximately 100 nm film deposited at 250 °C, multiple reflections originating from both the stable orthorhombic α [66] and metastable monoclinic β [67] phases of MoO_3 were detected by grazing incidence XRD (Fig. 4a). In addition, a strong reflection was detected at approximately 22.4° 2θ accompanied by a second reflection close to 46° 2θ, which corresponds to half the d-spacing of the first peak. These peaks could not be indexed to either of the MoO_3 phases. Instead, several known suboxide phases, including γ-Mo_4O_{11}, [68] η-Mo_4O_{11} [69], $Mo_{17}O_{47}$ [70], Mo_5O_{14} [71], Mo_8O_{23} [72], Mo_9O_{26} [73], and $Mo_{18}O_{52}$ [74] have reflections close to these positions. The three partially overlapping peaks at 22.4 (suboxide), 23.0 [β-MoO_3 (011)] and 23.3 °2θ [α-MoO_3 (110)] were the most intense for each phase also in the θ–2θ geometry (Fig. S2, Supplementary data) and the relative peak intensities were also rather similar to the GIXRD measurements. Thus, taking into account the well-known differences between GIXRD and θ–2θ geometries and the planes detected by them [75], none of the phases appears to be strongly textured.

Raman spectroscopy was also used to study the phase composition. α [76,77] and β [77] phases of MoO_3 were detected with UV (325 nm), green (532 nm), and red (633 nm) lasers, although the relative intensities of the peaks were different for each laser (Fig. 4b). However, no signs of any suboxide phase were seen with any of the lasers. Both γ-Mo_4O_{11} and η-Mo_4O_{11} have been reported to be relatively weakly Raman active when excited with a green (514.5 or 532 nm) laser [78,79], but increased Raman activity under red (633 nm) laser illumination has been noted for these phases [78,80]. $Mo_{18}O_{52}$ has been reported to be weakly Raman active under IR (1064 nm), red (633 nm), and UV (244 nm) lasers, whereas relatively strong peaks should result from Mo_8O_{23} when using either a 633 or 244 nm laser [80]. To the best of our knowledge, Raman spectra of other suboxide phases, such as $Mo_{17}O_{47}$, Mo_5O_{14}, or Mo_9O_{26}, have not been reported.

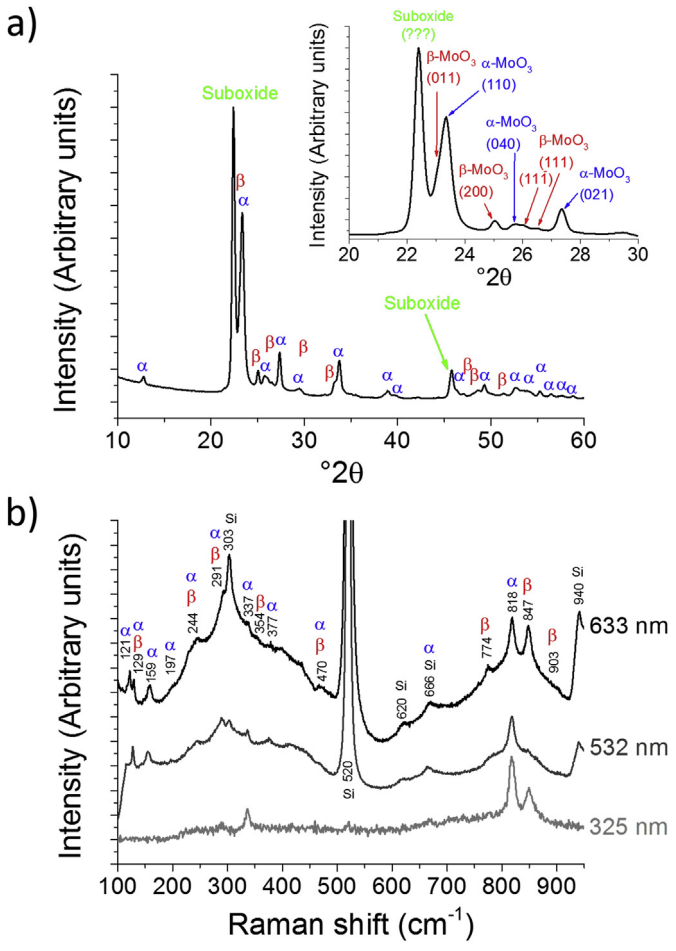

Fig. 4. (a) Grazing incidence X-ray diffractograms. The inset shows the region from 20 to 30 °2θ in more detail with Miller indices of the peaks. (b) Raman spectra measured with different lasers. α and β refer to α-MoO_3 and β-MoO_3, whereas suboxide denotes an unidentified MoO_x ($2.75 \leq x \leq 2.89$) phase. The MoO_x films were deposited on silicon at 250 °C using 1000 cycles.

Deposition temperature had a strong effect on film morphology (Fig. 5) as well as crystallinity (Fig. 6). The film deposited at 200 °C appeared smooth and nearly featureless, in line with its amorphous structure. At 225 °C rod-like crystallites of an unidentified suboxide phase formed. The films deposited between 240 and 255 °C had rather similar morphologies with rough surfaces composing of both rod and plate-like crystallites, and the films contained both the α and β phases of MoO_3 in addition to the suboxide phase(s). At 260 °C plate-like crystallites started to dominate the surface, which was accompanied by a strong decrease in the XRD reflection originating from the suboxide ($2\theta \approx 22.4°$), while both MoO_3 phases were still present. The dominantly plate-like films deposited at 275–300 °C were nearly phase-pure α-MoO_3 with slight traces of β-MoO_3. In addition, the changes in the relative intensities of the α-MoO_3 peaks at temperatures above 260 °C suggest changes in their orientation.

We also observed that precursor pulse times had some effect on the film morphology and phase composition: long $MoO_2(thd)_2$ pulses led to more plate-like morphology with increased amount of α-MoO_3 compared to the suboxide and β-MoO_3 (Fig. S3, Supplementary data), whereas long O_3 pulses decreased the amount of the suboxide with a corresponding increase in both the α- and β-MoO_3 phases (Fig. S4, Supplementary data). Even purge times affected film morphology (Fig. S5, Supplementary data). There are at least two ways the pulse times may affect the film morphology and crystallinity at doses higher than those needed for saturation of the growth rate. First, longer pulses or purges give more time for processes such as crystallization, phase transformation, and surface diffusion. Second, increasing the dose of especially the reactant, such as ozone, may reduce the impurities, improve the stoichiometry, and affect the film structure.

Notable changes in the film morphology (Fig. 7a and Fig. S6, Supplementary data) as well as crystallinity (Fig. 7b) occurred at 250 °C with increasing film thickness. The thinnest films up to 100 cycles were smooth and amorphous, whereas a crystalline suboxide phase was formed after 250 cycles, which was accompanied by a strong increase in roughness. Thereafter the roughness continued to increase up to 1000 cycles, and changes in phase composition were also observed: both α- and β-MoO_3 formed after 500 cycles and their amounts relative to the suboxide seemed to increase with increasing film thickness. The observation of onset of crystallization between 100 and 250 cycles agrees well with the strong increase in the growth rate discussed in Section 3.1. The roughness of the films increases their surface area, which has been found beneficial in many applications of MoO_x, as discussed in the Introduction. Based on AFM images, the surface area of the roughest, 1000 cycle film was estimated to be approximately twice the substrate area.

The films deposited at 225, 250, and 275 °C were all relatively pure. The main impurity was hydrogen, and some carbon and nitrogen were also detected (Table 1). The O/Mo ratios were rather close to 3; this probably results from a balance of the suboxide MoO_x phase ($2.75 \leq x \leq 2.89$) decreasing the ratio and the presence

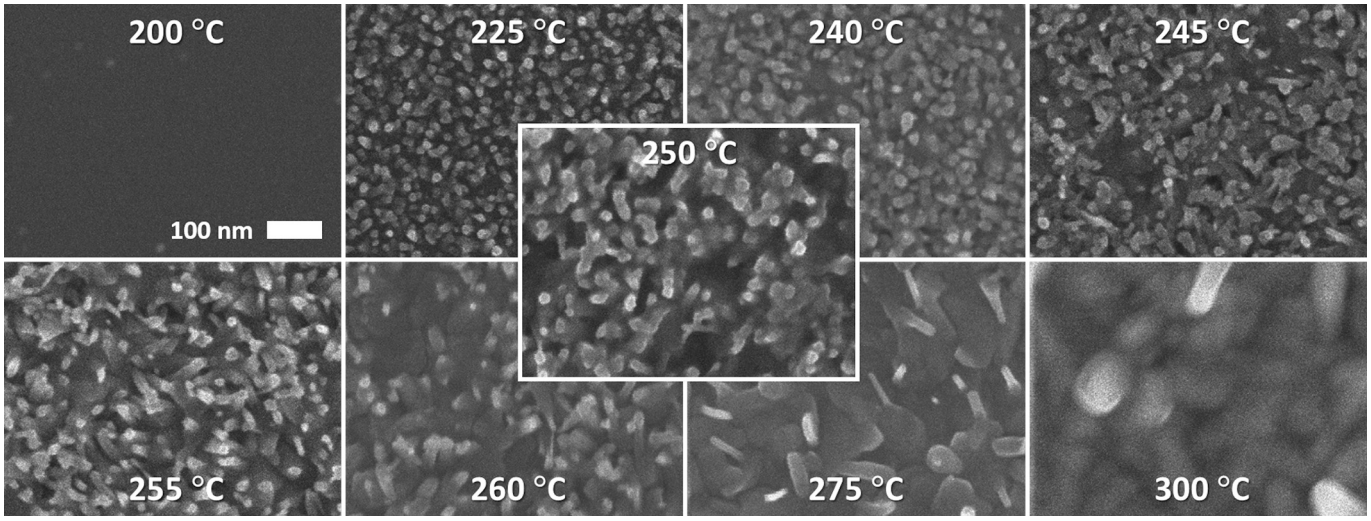

Fig. 5. SEM images of MoO_x films deposited on silicon at different temperatures using 1000 cycles.

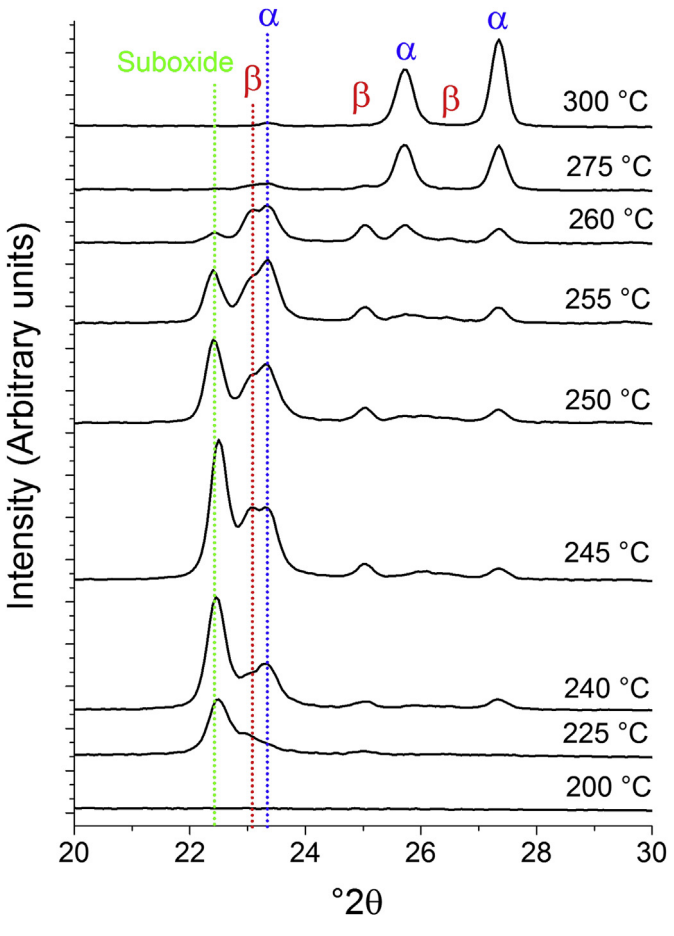

Fig. 6. Grazing incidence X-ray diffractograms of MoO_x films deposited on silicon at different temperatures using 1000 cycles. α and β refer to α-MoO_3 and β-MoO_3, whereas suboxide denotes an unidentified MoO_x ($2.75 \leq x \leq 2.89$) phase.

of residual OH^- groups increasing it. The highest hydrogen content was measured for the film deposited at 250 °C, which also had the highest O/Mo ratio, suggesting the incorporation of hydrogen as hydroxyl groups. The amount of carbon, which likely originates from the precursor, was low and decreased with increasing deposition temperature. Interestingly, the films contained small amounts of N (0.5–1 at-%). We think this has to be incorporated during the deposition from the usually inert N_2 carrier gas, as no nitrogen-containing chemicals were used in the precursor synthesis and the nitrogen appears to be distributed throughout the film thickness. Molybdenum oxides have been reported to incorporate nitrogen relatively easily. For example, films deposited from a nitrogen-containing precursor $MoO_2(^tBuAMD)_2$ and O_3 by ALD were described as Mo(VI)oxynitride [52], partial nitridation of MoO_x has been reported upon N_2 annealing at 400 °C [81], and nitrogen impurities have also been found for MoO_x films deposited under nominally nitrogen-free conditions [12].

X-ray photoelectron spectroscopy (XPS) showed that molybdenum on the film surface was mostly present as Mo^{6+}, as evidenced by the Mo $3d_{5/2}$ and Mo $3d_{3/2}$ binding energies of 233.0 and 236.2 eV, respectively (Fig. 8a). Approximately 10% of molybdenum was identified as Mo^{5+} represented by a doublet with binding energies of 231.3 (Mo $3d_{5/2}$) and 234.5 eV (Mo $3d_{3/2}$). The observed binding energies are within the range reported for different MoO_3 samples [82], in particular close to the values for crystalline ALD α-MoO_3 films deposited by Vos et al. [51] and somewhat higher than those reported for amorphous ALD MoO_3 [49,53,56]. The Mo^{5+} content would be expected to range from 50% (Mo_4O_{11}) to 22% (Mo_9O_{26}) for the different suboxide phases. However, the similar Mo^{5+}/Mo^{6+} ratios for the films deposited at different temperatures point to changes on the film surface due to ambient exposure, as XRD showed the films deposited at 225 and 275 °C to be nearly phase-pure suboxide and α-MoO_3, respectively.

The majority of oxygen (Fig. 8b) was present as oxide ions (O^{2-}), whereas about 5% (275 °C) or 12% (225 and 250 °C) of oxygen was identified as hydroxyl groups (OH^-). The O 1s binding energies of 530.7 (O^{2-}) and 531.9 eV (OH^-) are in relatively good agreement with other ALD MoO_3 films [49,51,56]. A minor O 1s component at 533.3 eV was attributed to organic species containing oxygen, in accordance with detection of carbonyl species in C 1s spectra (not shown).

Optical properties were evaluated from the films deposited on soda lime glass substrates. Using a Tauc plot, an indirect band gap of 2.8 eV was extracted for a 2000 cycle film deposited at 250 °C (Fig. S7, Supplementary data), which is within the range of band gap values (2.7–3.2 eV) reported for MoO_3 [1,7,51,83]. The refractive indices at 580 nm ranged from 2.0 for the amorphous films to 2.2 for the predominantly α-MoO_3 films deposited at 275–300 °C and

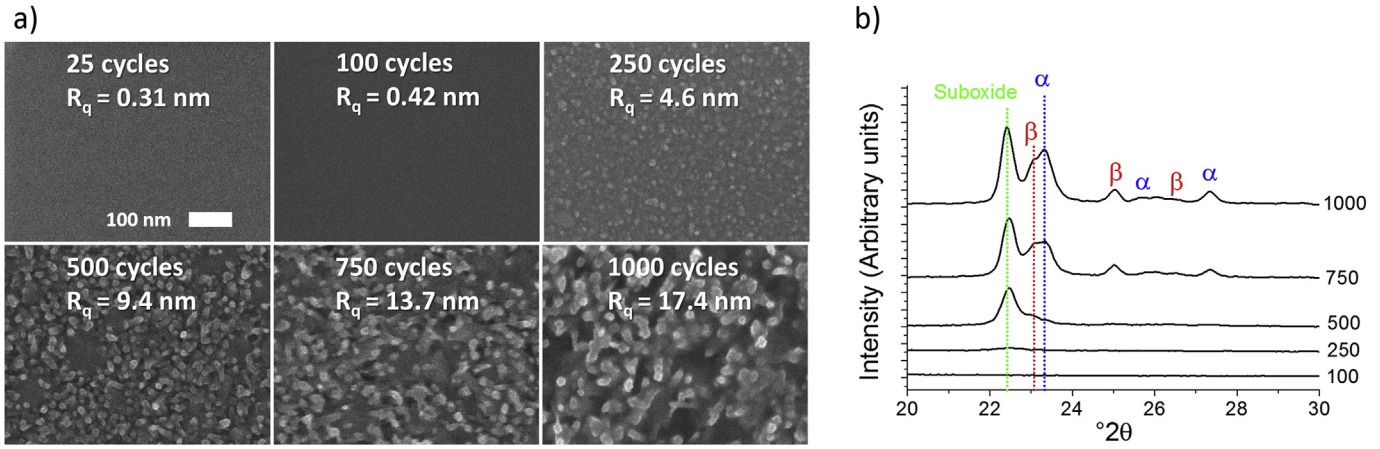

Fig. 7. (a) SEM images and roughness values (R_q) measured by AFM and (b) grazing incidence X-ray diffractograms of MoO_x films of different thicknesses deposited on silicon at 250 °C. α and β refer to α-MoO_3 and β-MoO_3, whereas suboxide denotes an unidentified MoO_x ($2.75 \leq x \leq 2.89$) phase.

Table 1
Elemental compositions analyzed by ToF-ERDA for MoO_x films deposited at different temperatures on silicon using 1000 cycles.

Deposition temperature (°C)	Mo (at-%)	O (at-%)	O/Mo	C (at-%)	H (at-%)	N (at-%)
225	24.0 ± 1.2	71.2 ± 2.9	2.97 ± 0.19	1.3 ± 0.5	3.0 ± 1.2	0.58 ± 0.24
250	22.0 ± 0.5	70.1 ± 1.3	3.19 ± 0.10	0.47 ± 0.15	6.6 ± 1.1	0.92 ± 0.15
275	24.4 ± 1.0	73.2 ± 2.4	3.01 ± 0.16	0.11 ± 0.07	1.8 ± 0.8	0.56 ± 0.22

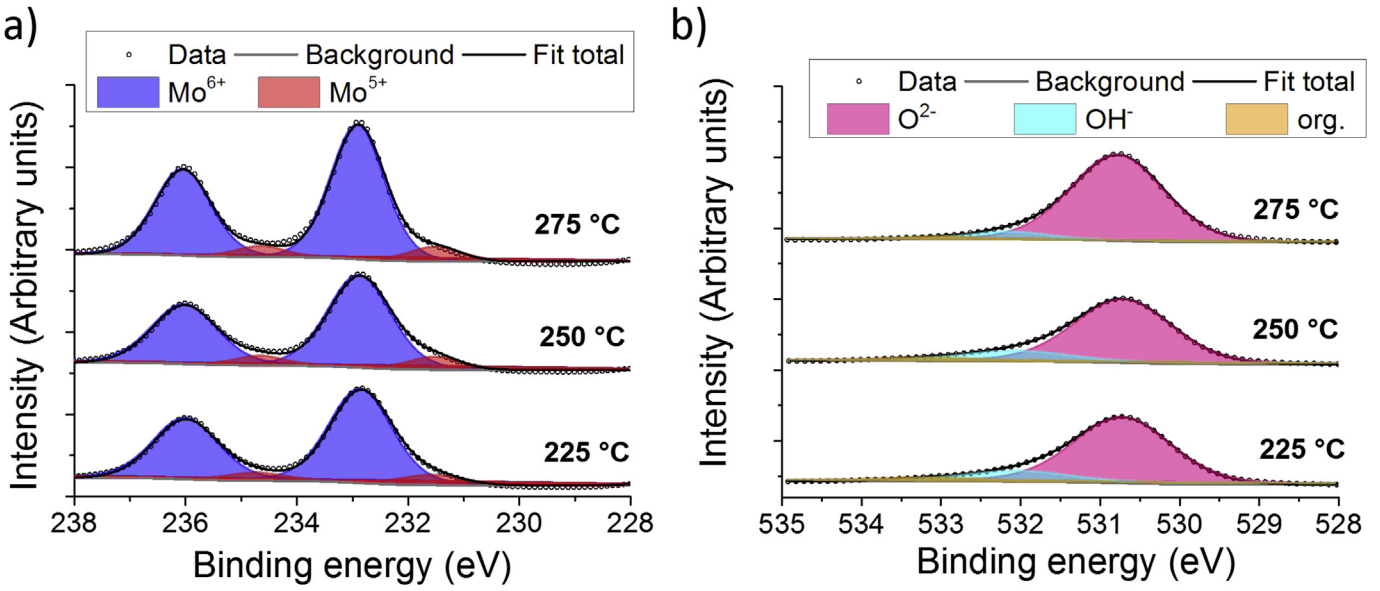

Fig. 8. X-ray photoelectron spectra of (a) Mo 3d and (b) O 1s regions of MoO_x films deposited at different temperatures on silicon using 1000 cycles.

even 2.4–2.5 for the mixed-phase films deposited at 250 °C. Refractive indices ranging from 1.8 to 2.2 have been reported for trioxide-like MoO_x films [7,51,83]. Thus, the highest values measured for the mixed-phase films may be due to the suboxide phase(s).

3.3. Post-deposition annealing

The phase composition of the MoO_x films could be tuned by changing the deposition conditions. However, the majority of the deposited films were mixtures of three phases. Additional control in phase composition was sought through post-deposition annealing. Approximately 100 nm thick MoO_x films deposited at 250 °C (1000 cycles), which consisted of a mixture of suboxide, α-MoO_3, and β-MoO_3 phases, were selected for annealing experiments performed in both oxidizing and reducing atmospheres. The effects of annealing were followed *in situ* by HTXRD.

Upon annealing in O_2 the first changes occurred above 306 and 346 °C, when the suboxide and metastable β-MoO_3 phases, respectively, disappeared (Fig. 9). From 386 to 586 °C the film was phase-pure α-MoO_3, the only changes being peak shifts due to anisotropic thermal expansion and variation in relative peak intensities (preferred orientation). Above 586 °C, the α-MoO_3 film sublimed, leaving a bare silicon substrate, as verified by EDS. The

onset temperature for the sublimation of α-MoO_3 has been reported to be 500–700 °C depending on experimental conditions [84,85]. Attempts to produce ultrathin, 2D α-MoO_3 films from amorphous, sub-5 nm MoO_x films were unsuccessful, as no crystallization was detected by either *in situ* or *ex situ* XRD after annealing in O_2 to 450 °C or higher temperatures.

Forming gas (10% H_2/90% N_2) provided a reducing atmosphere in order to produce MoO_2 films. The first changes in HTXRD measurements were observed above 226 °C (Fig. 10), when β-MoO_3 disappeared and the initial suboxide phase transformed to a new phase, most likely monoclinic η-Mo_4O_{11} [69]. At 386 °C, η-Mo_4O_{11} may have converted to another suboxide phase and α-MoO_3 had disappeared with MoO_2 starting to form. The formation of η-Mo_4O_{11} is further supported by isothermal measurements presented later in this section. Between 426 and 546 °C, the film was phase-pure, monoclinic MoO_2 (tugarinovite) [86]. Starting at 586 °C, MoO_2 disappeared and a few broad reflections appeared that most likely originate from molybdenum silicide(s).

An HTXRD experiment was also performed in air, which yielded results very similar to O_2 (not shown). Annealing in N_2, on the other hand, produced a complex mixture of MoO_x phases (Fig. S8, Supplementary data). Multiple peaks arising from suboxide phase(s) appeared at 386 °C. β-MoO_3 disappeared by 426 °C and α-MoO_3 by 626 °C leaving only the suboxide phase(s) between 626 and 666 °C, where the heating was stopped.

Further insight into the production of phase-pure α-MoO_3 and MoO_2 films in O_2 and forming gas, respectively, was obtained through isothermal HTXRD measurements. The transformation to α-MoO_3 was rapid in O_2 atmosphere at 450 °C; only α-MoO_3 was detected after annealing for 35 min and no changes in peak intensities were seen when the annealing was continued (Fig. S9, Supplementary data). MoO_2 formed more slowly in forming gas at 450 °C (Fig. S10, Supplementary data): after 35 min of annealing β-MoO_3 and the initial suboxide phase had disappeared, but α-MoO_3 remained and an intermediate phase identified as η-Mo_4O_{11} [69] had formed along with some traces of MoO_2. The η-Mo_4O_{11} intermediate, which has been commonly observed when reducing MoO_3 to MoO_2 [87,88], was completely removed and formation of MoO_2 finished after annealing for 140 min. Further annealing caused no changes in the diffractograms.

3.4. Characterization of annealed films

The MoO_2 films formed by annealing in forming gas at 450 °C had a very rough morphology consisting of flower-like structures with widths of about 1 μm (Fig. 11a). Between these structures a smoother area was exposed. The α-MoO_3 films formed by the O_2 annealing at 450 °C consisted of plate-like crystallites on the surface with roughness comparable to the as-deposited film (Fig. 11b). The film formed after the HTXRD measurement in forming gas ending at 666 °C was found to be a mixture of tetragonal α-$MoSi_2$ and Mo_5Si_3 phases with an additional reflection that we were unable to identify (Fig. S11a, Supplementary data). The morphology and roughness of this film were rather similar to the as-deposited film (Fig. S11b, Supplementary data). The formation of silicides is attributed to reactions between the film and the silicon substrate. It is plausible that MoO_2 is first reduced to metallic Mo, which has been reported to occur, although very slowly, at temperatures as low as 500 °C in 10% H_2 [87]. $MoSi_x$ is then formed upon reaction of Mo film with the Si substrate, which has been reported to proceed at 500 °C and above [89]. Therefore, it seems that metallic Mo films could be obtained upon reduction in forming gas at approximately 600 °C if the Si substrate was covered by a suitable diffusion barrier layer.

The α-MoO_3 film produced by annealing in O_2 showed lower levels of H and N compared to the as-deposited film, with slightly over stoichiometric O/Mo ratio of 3.15 ± 0.11 (Table 2). The MoO_2 film resulting from annealing in forming gas had an O/Mo ratio of 2.11 ± 0.05 and the film was the purest of all analyzed films with sub-at-% carbon, nitrogen, and hydrogen contents. Whereas ToF-ERDA provides results averaged through the whole film thickness, the surface was specifically probed by XPS.

The as-deposited and oxygen-annealed films appeared to have nearly identical surface composition with some 90% of Mo present as Mo^{6+} and 10% as Mo^{5+} (Fig. S12a, Supplementary data). The O 1s component at 531.9 eV attributed to hydroxyl groups, however, was approximately halved by the O_2 annealing (Fig. S12b). Mo^{4+} was expectedly detected after the forming gas annealing with Mo $3d_{5/2}$ and $3d_{3/2}$ binding energies of 229.7 and 232.9 eV, respectively, although the relative amounts of Mo^{4+}, Mo^{5+}, and Mo^{6+} were approximately identical on the surface. This is likely due to surface

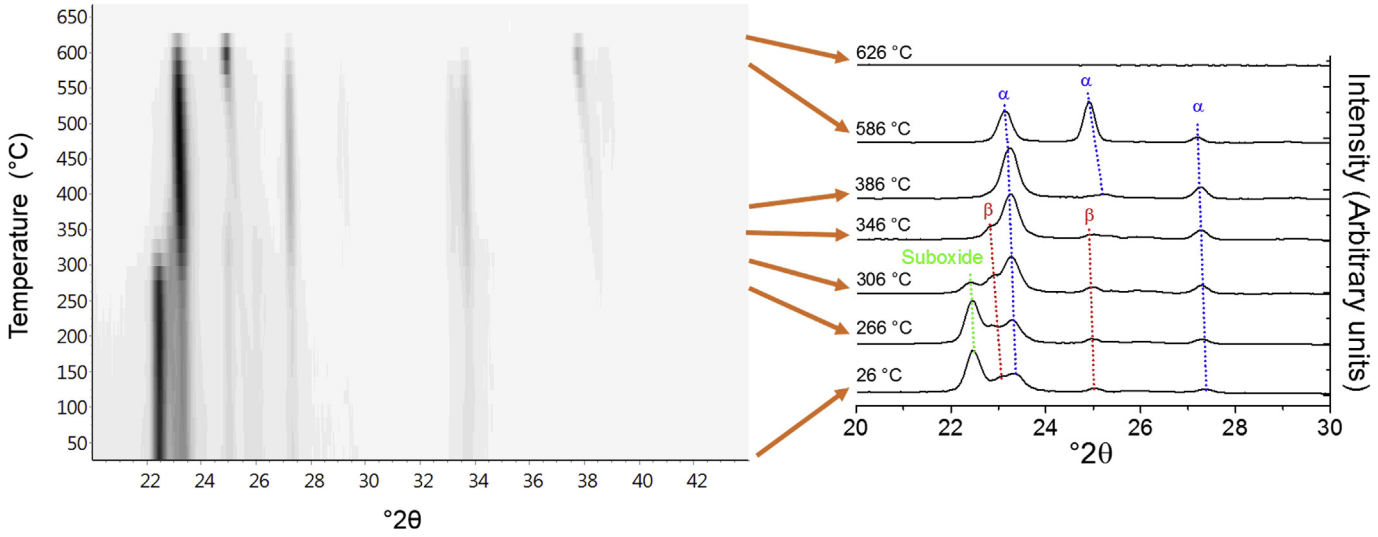

Fig. 9. High-temperature grazing incidence X-ray diffractograms (left) of a MoO_x film heated in O_2 from 26 to 666 °C, where white and black represent low and high intensities, respectively. On right, peaks between 20 and 30 °2θ are identified at selected temperatures to highlight the phase transitions. α and β refer to α-MoO_3 and β-MoO_3, whereas suboxide denotes an unidentified MoO_x ($2.75 \leq x \leq 2.89$) phase.

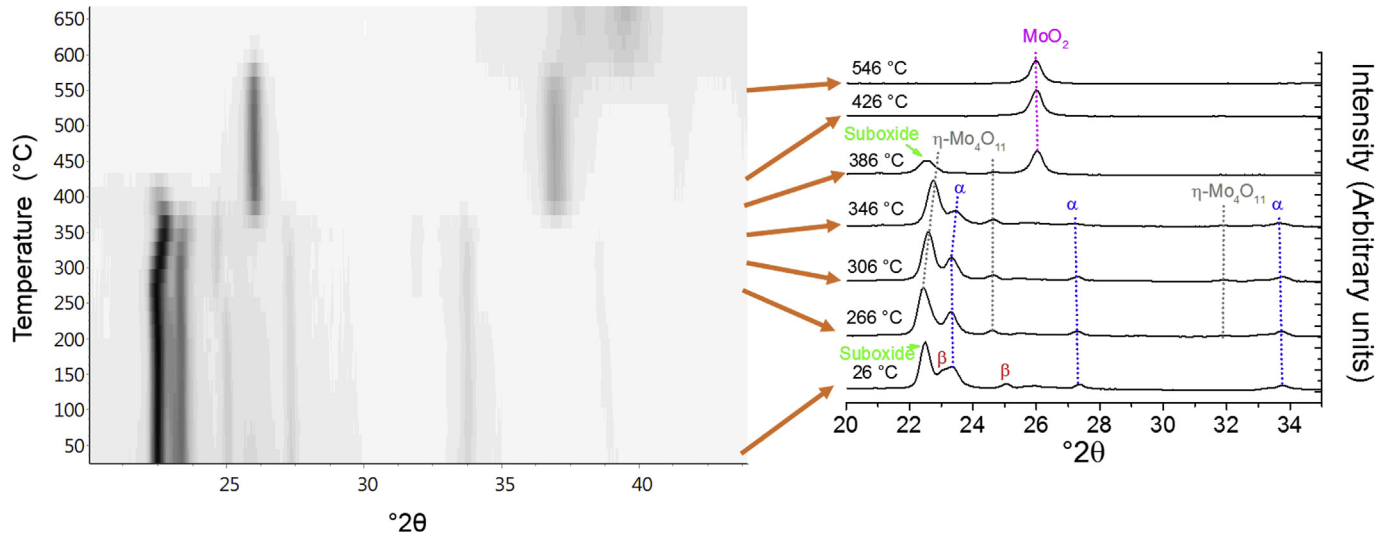

Fig. 10. High-temperature grazing incidence X-ray diffractograms (left) of a MoO_x film heated in forming gas (10% H_2/90% N_2) from 26 to 666 °C, where white and black represent low and high intensities, respectively. On right, peaks between 20 and 35 °2θ are identified at selected temperatures to highlight the phase transitions. α and β refer to α-MoO_3 and β-MoO_3, whereas suboxide denotes an unidentified MoO_x ($2.75 \leq x \leq 2.89$) phase.

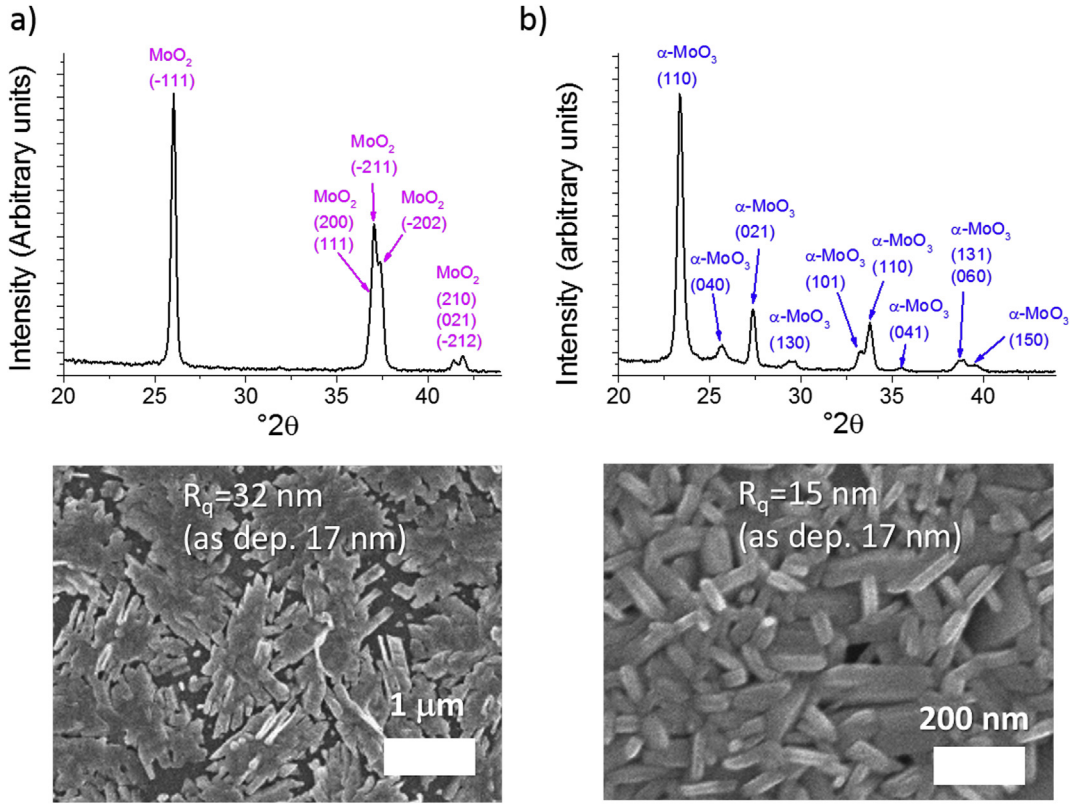

Fig. 11. Grazing incidence X-ray diffractograms (top row) and SEM images together with roughness values measured by AFM (bottom row) of (a) MoO_2 film produced by annealing in forming gas (450 °C, 3 h) and (b) α-MoO_3 film produced by annealing in O_2 (450 °C, 1 h).

Table 2
Elemental compositions of annealed MoO_x films analyzed by ToF-ERDA. The films were deposited on silicon at 250 °C using 1000 cycles.

Treatment	Mo (at-%)	O (at-%)	O/Mo	C (at-%)	H (at-%)	N (at-%)
As-deposited (250 °C)	22.0 ± 0.5	70.1 ± 1.3	3.19 ± 0.10	0.47 ± 0.15	6.6 ± 1.1	0.92 ± 0.15
O_2 annealed (450 °C, 1 h)	23.5 ± 0.6	74.0 ± 1.5	3.15 ± 0.11	0.53 ± 0.13	1.9 ± 0.6	0.12 ± 0.04
Forming gas annealed (450 °C, 3 h)	31.8 ± 0.6	67.1 ± 1.1	2.11 ± 0.05	0.59 ± 0.16	0.12 ± 0.03	0.40 ± 0.11

oxidation of the MoO_2 film, as has been previously observed [82]. Interestingly, the relative intensity of the 531.9 eV O 1s peak attributed to the OH^- groups increased after the forming gas annealing, although the hydrogen content throughout the film analyzed by ToF-ERDA was negligible. This suggests that the hydroxyl groups may have been exclusively present on the film surface in the forming gas annealed film, perhaps due to exposure to ambient air.

4. Conclusions

Atomic layer deposition of crystalline molybdenum oxide thin films was demonstrated using a new, commercially available precursor $MoO_2(thd)_2$ with O_3. Well controlled film growth with good uniformity and conformality was achieved although complete saturation was not reached with $MoO_2(thd)_2$. Most of the films were mixtures of α-MoO_3, β-MoO_3, and an unidentified suboxide MoO_x phase ($2.75 \leq x \leq 2.89$). The film composition was close to MoO_3 and the films had fairly low levels of impurities. Relative amounts of the different phases could be controlled by changing the deposition conditions. Post-deposition annealing treatments studied by high-temperature X-ray diffraction enabled further control of film composition. In particular, single-phase α-MoO_3 and MoO_2 films were achieved by annealing in O_2 and forming gas, respectively. As the thickness, crystallinity, morphology, and phase composition strongly affect the performance of MoO_x films, the presented ALD process constitutes an important step towards the use of MoO_x in various applications such as sensing, energy storage, and catalysis.

Declarations of interest

None.

Acknowledgements

The research was supported by the Finnish Centre of Excellence in Atomic Layer Deposition funded by Academy of Finland and ASM Microchemistry. Ms. Kati Meriläinen and Mr. Mikko Kaipio are acknowledged for their help with the Raman and HTXRD measurements, respectively. Mr. Niklas Stegmann is thanked for assistance in thickness measurements and Mr. Tomi Iivonen and Mr. Georgi Popov are acknowledged for helping with the UV–VIS measurements.

Appendix A. Supplementary data

Supplementary data related to this article can be found at https://doi.org/10.1016/j.mtchem.2018.04.005.

References

[1] I.A. de Castro, R.S. Datta, J.Z. Ou, A. Castellanos-Gomez, S. Sriram, T. Daeneke, K. Kalantar-zadeh, Molybdenum oxides – from fundamentals to functionality, Adv. Mater. 29 (2017) 1701619.
[2] L. Kihlborg, Studies on molybdenum oxides, Acta Chem. Scand. 13 (1959) 954–962.
[3] L. Kihlborg, The crystal chemistry of molybdenum oxides, in: R. Ward (Ed.), Advances in Chemistry: Nonstoichiometric Compounds, American Chemical Society, Washington, D.C., 1963, pp. 37–45.
[4] H. Vincent, M. Mareio, On structural aspects of molybdenum bronzes and molybdenum oxides in relation to their low-dimensional transport properties, in: C. Schlenker (Ed.), Low-dimensional Electronic Properties of Molybdenum Bronzes and Oxides, Kluwer Academic Publishers, Dordrecht, The Netherlands, 1989, pp. 49–86.
[5] P.F. Carcia, E.M. McCarron, Synthesis and properties of thin film polymorphs of molybdenum trioxide, Thin Solid Films 155 (1987) 53–63.
[6] I. Navas, R. Vinodkumar, K.J. Lethy, A.P. Detty, V. Ganesan, V. Sathe, V.P. Mahadevan Pillai, Growth and characterization of molybdenum oxide nanorods by RF magnetron sputtering and subsequent annealing, J. Phys. D Appl. Phys. 42 (2009) 175305.
[7] N. Miyata, S. Akiyoshi, Preparation and electrochromic properties of rf-sputtered molybdenum oxide films, J. Appl. Phys. 58 (1985) 1651–1655.
[8] R.L. Smith, G.S. Rohrer, Scanning probe microscopy of cleaved molybdates: α-MoO_3(010), $Mo_{18}O_{52}$(100), Mo_8O_{23}(010), and η-Mo_4O_{11}(100), J. Solid State Chem. 124 (1996) 104–115.
[9] M.S. da Luz, A. de Campos, B.D. White, J.J. Neumeier, Electrical resistivity, high-resolution thermal expansion, and heat capacity measurements of the charge-density wave compound y-Mo_4O_{11}, Phys. Rev. B 79 (2009) 233106.
[10] D.B. Rogers, R.D. Shannon, A.W. Sleight, J.L. Gillson, Crystal chemistry of metal dioxides with rutile-related structures, Inorg. Chem. 8 (1969) 841–849.
[11] S. Balendhran, J. Deng, J.Z. Ou, S. Walia, J. Scott, J. Tang, K.L. Wang, M.R. Field, S. Russo, S. Zhuiykov, M.S. Strano, N. Medhekar, S. Sriram, M. Bhaskaran, K. Kalantar-zadeh, Enhanced charge carrier mobility in two-dimensional high dielectric molybdenum oxide, Adv. Mater. 25 (2013) 109–114.
[12] K. Inzani, M. Nematollahi, F. Vullum-Bruer, T. Grande, T.W. Reenaas, S.M. Selbach, Electronic properties of reduced molybdenum oxides, Phys. Chem. Chem. Phys. 19 (2017) 9232–9245.
[13] T. He, J. Yao, Photochromism of molybdenum oxide, J. Photochem. Photobiol. C Photochem. Rev. 4 (2003) 125–143.
[14] X.K. Hu, Y.T. Qian, Z.T. Song, J.R. Huang, R. Cao, J.Q. Xiao, Comparative study on MoO_3 and H_xMoO_3 nanobelts: structure and electric transport, Chem. Mater. 20 (2008) 1527–1533.
[15] J. Scarminio, A. Lourenço, A. Gorenstein, Electrochromism and photochromism in amorphous molybdenum oxide films, Thin Solid Films 302 (1997) 66–70.
[16] M. Rouhani, J. Hobley, G.S. Subramanian, I.Y. Phang, Y.L. Foo, S. Gorelik, The influence of initial stoichiometry on the mechanism of photochromism of molybdenum oxide amorphous films, Sol. Energy Mater. Sol. Cells 126 (2014) 26–35.
[17] J.H. Ku, J.H. Ryu, S.H. Kim, O.H. Han, S.M. Oh, Reversible lithium storage with high mobility at structural defects in amorphous molybdenum dioxide electrode, Adv. Funct. Mater. 22 (2012) 3658–3664.
[18] S.K. Deb, J.A. Chopoorian, Optical properties and color-center formation in thin films of molybdenum trioxide, J. Appl. Phys. 37 (1966) 4818–4825.
[19] M.A. Arvizu, M. Morales-Luna, M. Pérez-González, E. Campos-Gonzalez, O. Zelaya-Angel, S.A. Tomás, Influence of thermal annealings in argon on the structural and thermochromic properties of MoO_3 thin films, Int. J. Thermophys. 38 (2017) 51.
[20] S.S. Kanu, R. Binions, Thin films for solar control applications, Proc. R. Soc. A Math. Phys. Eng. Sci. 466 (2009) 19–44.
[21] Y. Ohko, T. Tatsuma, T. Fujii, K. Naoi, C. Niwa, Y. Kubota, A. Fujishima, Multicolour photochromism of TiO_2 films loaded with silver nanoparticles, Nat. Mater. 2 (2003) 29–31.
[22] J.N. Yao, K. Hashimoto, A. Fujishima, Photochromism induced in an electrolytically pretreated MoO_3 thin film by visible light, Nature 355 (1992) 624–626.
[23] M.M. Bettahar, G. Costentin, L. Savary, J.C. Lavalley, On the partial oxidation of propane and propylene on mixed metal oxide catalysts, Appl. Catal. A Gen. 145 (1996) 1–48.
[24] G. Mestl, T.K.K. Srinivasan, Raman spectroscopy of monolayer-type catalysts: supported molybdenum oxides, Catal. Rev. Sci. Eng. 40 (1998) 451–570.
[25] S.S. Sunu, E. Prabhu, V. Jayaraman, K.I. Gnanasekar, T.K. Seshagiri, T. Gnanasekaran, Electrical conductivity and gas sensing properties of MoO_3, Sens. Actuators B 101 (2004) 161–174.
[26] M. Arita, H. Kaji, T. Fujii, Y. Takahashi, Resistance switching properties of molybdenum oxide films, Thin Solid Films 520 (2012) 4762–4767.
[27] N.A. Chernova, M. Roppolo, A.C. Dillon, M.S. Whittingham, Layered vanadium and molybdenum oxides: batteries and electrochromics, J. Mater. Chem. 19 (2009) 2526–2552.
[28] K.C. Santosh, R.C. Longo, R. Addou, R.M. Wallace, K. Cho, Electronic properties of MoS_2/MoO_x interfaces: implications in tunnel field effect transistors and hole contacts, Sci. Rep. 6 (2016) 33562.
[29] A.J. Molina-Mendoza, J.L. Lado, J.O. Island, M.A. Niño, L. Aballe, M. Foerster, F.Y. Bruno, A. López-Moreno, L. Vaquero-Garzon, H.S.J. van der Zant, G. Rubio-Bollinger, N. Agraït, E.M. Pérez, J. Fernández-Rossier, A. Castellanos-Gomez, Centimeter-scale synthesis of ultrathin layered MoO_3 by van der waals epitaxy, Chem. Mater. 28 (2016) 4042–4051.
[30] F. Ji, X. Ren, X. Zheng, Y. Liu, L. Pang, J. Jiang, S. Liu, 2D-MoO_3 nanosheets for superior gas sensors, Nanoscale 8 (2016) 8696–8703.
[31] O.G. Marin Flores, S. Ha, Activity and stability studies of MoO_2 catalyst for the partial oxidation of gasoline, Appl. Catal. A Gen. 352 (2009) 124–132.
[32] Y. Shi, B. Guo, S.A. Corr, Q. Shi, Y.-S. Hu, K.R. Heier, L. Chen, R. Seshadri, G.D. Stucky, Ordered mesoporous metallic MoO_2 materials with highly reversible lithium storage capacity, Nano Lett. 9 (2009) 4215–4220.
[33] L. Zhou, N. Ding, J. Yang, L. Yang, Y. Zong, Z. Liu, A. Yu, Sulfur encapsulated in Mo_4O_{11}-anchored ultralight graphene for high-energy lithium sulfur batteries, ACS Sustain. Chem. Eng. 4 (2016) 3679–3687.
[34] E. Shembel, R. Apostolova, V. Nagirny, I. Kirsanova, P. Grebenkin, P. Lytvyn, Electrolytic molybdenum oxides in lithium batteries, J. Solid State Electrochem. 9 (2005) 96–105.
[35] P.A. Christian, J.N. Carides, F.J. DiSalvo, J.V. Waszczak, Molybdenum oxide cathodes in secondary lithium cells, J. Electrochem. Soc. 127 (1980) 2315–2319.
[36] B. Delmon, Solid state reactions in catalysts: an approach to real active systems and their deactivation, in: C.H. Bartholomew, G.A. Fuentes (Eds.), Studies

in Surface Science and Catalysis, vol. 111, Elsevier B.V., Amsterdam, Netherlands, 1997, pp. 39–51.
[37] E.M. Gaigneaux, M.J. Genet, P. Ruiz, B. Delmon, Catalytic behavior of molybdenum suboxides in the selective oxidation of isobutene to methacrolein, J. Phys. Chem. B 104 (2000) 5724–5737.
[38] D. Di Yao, J.Z. Ou, K. Latham, S. Zhuiykov, A.P. O'Mullane, K. Kalantar-zadeh, Electrodeposited α- and β-phase MoO_3 films and investigation of their gasochromic properties, Cryst. Growth Des. 12 (2012) 1865–1870.
[39] C.J. Machiels, W.H. Cheng, U. Chowdhry, W.E. Farneth, F. Hong, E.M. McCarron, A.W. Sleight, The effect of the structure of molybdenum oxides on the selective oxidation of methanol, Appl. Catal. 25 (1986) 249–256.
[40] Z. Luo, R. Miao, T.D. Huan, I.M. Mosa, A.S. Poyraz, W. Zhong, J.E. Cloud, D.A. Kriz, S. Thanneeru, J. He, Y. Zhang, R. Ramprasad, S.L. Suib, Mesoporous MoO_{3-x} material as an efficient electrocatalyst for hydrogen evolution reactions, Adv. Energy Mater. 6 (2016).
[41] V.S. Saji, C.W. Lee, Molybdenum, molybdenum oxides, and their electrochemistry, ChemSusChem 5 (2012) 1146–1161.
[42] N. Illyaskutty, H. Kohler, T. Trautmann, M. Schwotzer, V.P. Mahadevan Pillai, Hydrogen and ethanol sensing properties of molybdenum oxide nanorods based thin films: effect of electrode metallization and humid ambience, Sensors Actuators B Chem. 187 (2013) 611–621.
[43] W. Li, F. Cheng, Z. Tao, J. Chen, Vapor-transportation preparation and reversible lithium intercalation/deintercalation of α-MoO_3 microrods, J. Phys. Chem. B 110 (2006) 119–124.
[44] M. Ritala, J. Niinistö, Atomic layer deposition, in: A.C. Jones, M.L. Hitchman (Eds.), Chemical Vapour Deposition: Precursors, Processes and Applications, Royal Society of Chemistry, Cambridge, 2009, pp. 158–206.
[45] S.M. George, Atomic layer deposition: an overview, Chem. Rev. 110 (2010) 111–131.
[46] M. Ritala, M. Leskelä, Atomic layer deposition, in: H.S. Nalwa (Ed.), Handbook of Thin Film Materials, Academic, San Diego, 2002, pp. 103–159.
[47] M. Diskus, O. Nilsen, H. Fjellvåg, Growth of thin films of molybdenum oxide by atomic layer deposition, J. Mater. Chem. 21 (2011) 705.
[48] J.-G. Song, G.H. Ryu, S.J. Lee, S. Sim, C.W. Lee, T. Choi, H. Jung, Y. Kim, Z. Lee, J.-M. Myoung, C. Dussarrat, C. Lansalot-Matras, J. Park, H. Choi, H. Kim, Controllable synthesis of molybdenum tungsten disulfide alloy for vertically composition-controlled multilayer, Nat. Commun. 6 (2015) 7817.
[49] A. Bertuch, G. Sundaram, M. Saly, D. Moser, R. Kanjolia, Atomic layer deposition of molybdenum oxide using bis(tert-butylimido)bis(dimethylamido) molybdenum, J. Vac. Sci. Technol. A 32 (2014), 01A119.
[50] B. Macco, M.F.J. Vos, N.F.W. Thissen, A.A. Bol, W.M.M. Kessels, Low-temperature atomic layer deposition of MoO_x for silicon heterojunction solar cells, Phys. Status Solidi Rapid Res. Lett. 9 (2015) 393–396.
[51] M.F.J. Vos, B. Macco, N.F.W. Thissen, A.A. Bol, W.M.M. Kessels, Atomic layer deposition of molybdenum oxide from $(N^tBu)_2(NMe_2)_2Mo$ and O_2 plasma, J. Vac. Sci. Technol. A 34 (2016), 01A103.
[52] A.R. Mouat, A.U. Mane, J.W. Elam, M. Delferro, T.J. Marks, P.C. Stair, Volatile hexavalent oxo-amidinate complexes: molybdenum and tungsten precursors for atomic layer deposition, Chem. Mater. 28 (2016) 1907–1919.
[53] T. Jurca, A.W. Peters, A.R. Mouat, O.K. Farha, J.T. Hupp, T.L. Lohr, M. Delferro, T.J. Marks, Second-generation hexavalent molybdenum oxo-amidinate precursors for atomic layer deposition, Dalton Trans. 46 (2017) 1172–1178.
[54] C.E. Nanayakkara, A. Vega, G. Liu, C.L. Dezelah, R.K. Kanjolia, Y.J. Chabal, Role of initial precursor chemisorption on incubation delay for molybdenum oxide atomic layer deposition, Chem. Mater. 28 (2016) 8591–8597.
[55] T.L. Drake, P.C. Stair, Vapor deposition of molybdenum oxide using bis(ethylbenzene) molybdenum and water, J. Vac. Sci. Technol. A 34 (2016) 51403.
[56] M. Diskus, O. Nilsen, H. Fjellvåg, S. Diplas, P. Beato, C. Harvey, E. van Schrojenstein Lantman, B.M. Weckhuysen, Combination of characterization techniques for atomic layer deposition MoO_3 coatings: from the amorphous to the orthorhombic α-MoO_3 crystalline phase, J. Vac. Sci. Technol. A 30 (2012), 01A107.
[57] T. Suntola, Atomic layer epitaxy, Thin Solid Films 216 (1992) 84–89.
[58] J. Jokinen, J. Keinonen, P. Tikkanen, A. Kuronen, T. Ahlgren, K. Nordlund, Comparison of TOF-ERDA and nuclear resonance reaction techniques for range profile measurements of keV energy implants, Nucl. Inst. Methods Phys. Res. B 119 (1996) 533–542.
[59] M. Mattinen, T. Hatanpää, T. Sarnet, K. Mizohata, K. Meinander, P.J. King, L. Khriachtchev, J. Räisänen, M. Ritala, M. Leskelä, Atomic layer deposition of crystalline MoS_2 thin films: new molybdenum precursor for low-temperature film growth, Adv. Mater. Interfaces 4 (2017) 1700213.
[60] B. Ballarin, E. Brescacin, G.A. Rizzi, E. Tondello, MoO_3 thin films prepared via MOCVD from a volatile molybdenyl complex, J. Mater. Chem. 5 (1995) 1147–1150.
[61] M. Nass, M. Schürmann, H. Preut, N. Krause, Crystal structure of cis-dioxo-bis(2,2,6,6-tetramethyl-3,5-heptandionato)-molybdenum(VI), $C_{22}H_{38}MoO_6$, Z. Kristallogr. New Cryst. Struct. 216 (2001) 461–464.
[62] Product catalog. Strem Chemicals, Inc. Available at: https://www.strem.com/catalog/. Accessed April 2018.
[63] A. Aarik, J. Karlis, H. Mändar, T. Uustare, V. Sammelselg, Influence of structure development on atomic layer deposition of TiO_2 thin films, Appl. Surf. Sci. 181 (2001) 339–348.
[64] W.D. Kim, G.W. Hwang, O.S. Kwon, S.K. Kim, M. Cho, D.S. Jeong, S.W. Lee, M.H. Seo, C.S. Hwang, Y.-S. Min, Y.J. Cho, Growth characteristics of atomic layer deposited TiO_2 thin films on Ru and Si electrodes for memory capacitor applications, J. Electrochem. Soc. 152 (2005). C552.
[65] S.K. Kim, S. Hoffmann-Eifert, M. Reiners, R. Waser, Relation between enhancement in growth and thickness-dependent crystallization in ALD TiO_2 thin films, J. Electrochem. Soc. 158 (2011). D6.
[66] Powder Diffraction File (PDF) 5-0508, JCPDS-ICDD, International Center for Diffraction Data, Newtown Square, PA.
[67] Powder Diffraction File (PDF) 47-1081, JCPDS-ICDD, International Center for Diffraction Data, Newtown Square, PA.
[68] Powder Diffraction File (PDF) 5-0337, JCPDS-ICDD, International Center for Diffraction Data, Newtown Square, PA.
[69] Powder Diffraction File (PDF) 13-0142, JCPDS-ICDD, International Center for Diffraction Data, Newtown Square, PA.
[70] Powder Diffraction File (PDF) 13-0345, JCPDS-ICDD, International Center for Diffraction Data, Newtown Square, PA.
[71] Powder Diffraction File (PDF) 12-0517, JCPDS-ICDD, International Center for Diffraction Data, Newtown Square, PA.
[72] Powder Diffraction File (PDF) 5-0339, JCPDS-ICDD, International Center for Diffraction Data, Newtown Square, PA.
[73] Powder Diffraction File (PDF) 5-0441, JCPDS-ICDD, International Center for Diffraction Data, Newtown Square, PA.
[74] Powder Diffraction File (PDF) 12-0753, JCPDS-ICDD, International Center for Diffraction Data, Newtown Square, PA.
[75] M. Birkholz, Thin Film Analysis by X-Ray Scattering, Wiley-VCH, Weinheim, Germany, 2005.
[76] M. Dieterle, G. Mestl, Raman spectroscopy of molybdenum oxides. Part I. Structural characterization of oxygen defects in MoO_{3-x} by DR UV/VIS, Raman spectroscopy and X-ray diffraction, Phys. Chem. Chem. Phys. 4 (2002) 812–821.
[77] T.M. McEvoy, K.J. Stevenson, Spatially resolved imaging of inhomogeneous charge transfer behavior in polymorphous molybdenum oxide. I. Correlation of localized structural, electronic, and chemical properties using conductive probe atomic force microscopy and Raman microprobe spectroscopy, Langmuir 21 (2005) 3521–3528.
[78] M. Dieterle, G. Mestl, Raman spectroscopy of molybdenum oxides. Part II. Resonance Raman spectroscopic characterisation of the molybdenum oxides Mo_4O_{11} and MoO_2, Phys. Chem. Chem. Phys. 4 (2002) 822–826.
[79] K. Olson, Laser Photodeposition of Molybdenum Oxide Thin Films from Organometallic Precursors (PhD thesis), Iowa State University, 1989.
[80] A. Blume, Synthese und strukturelle untersuchungen von molybdän- vanadium-, und wolfraoxide als referenzverbindungen Fur die heterogene katalyse (PhD thesis), 2004. TU Berlin.
[81] H. Wu, K. Lian, The development of pseudocapacitive molybdenum oxynitride electrodes for supercapacitors, ECS Trans. 58 (2014) 67–75.
[82] J. Baltrusaitis, B. Mendoza-Sanchez, V. Fernandez, R. Veenstra, N. Dukstiene, A. Roberts, N. Fairley, Generalized molybdenum oxide surface chemical state XPS determination via informed amorphous sample model, Appl. Surf. Sci. 326 (2015) 151–161.
[83] A. Szekeres, T. Ivanova, K. Gesheva, Spectroscopic ellipsometry study of CVD molybdenum oxide films: effect of temperature, J. Solid State Electrochem. 7 (2002) 17–20.
[84] S. Guimond, D. Göbke, J.M. Sturm, Y. Romanyshyn, H. Kuhlenbeck, M. Cavalleri, H.-J. Freund, Well-ordered molybdenum oxide layers on Au(111): preparation and properties, J. Phys. Chem. C 117 (2013) 8746–8757.
[85] M. Ferroni, V. Guidi, E. Comini, G. Sberveglieri, A. Vomiero, G. Della Mea, G. Martinelli, Selective sublimation processing of a molybdenum–tungsten mixed oxide thin film, J. Vac. Sci. Technol. B 21 (2003) 1442–1448.
[86] Powder Diffraction File (PDF) 32-0671, JCPDS-ICDD, International Center for Diffraction Data, Newtown Square, PA.
[87] T. Ressler, R.E. Jentoft, J. Wienold, M.M. Günter, O. Timpe, In situ XAS and XRD studies on the formation of Mo suboxides during reduction of MoO_3, J. Phys. Chem. B 104 (2000) 6360–6370.
[88] J. Dang, G.H. Zhang, K.C. Chou, Phase transitions and morphology evolutions during hydrogen reduction of MoO_3 to MoO_2, High Temp. Mater. Process. 33 (2014) 305–312.
[89] R.J. Nemanich, Phase formation during reactive molybdenum-silicide formation, J. Mater. Res. 5 (1990) 2854–2864.